Solution Structure of Pardaxin P-2†

Michael G. Zagorski,*,‡ David G. Norman,‡ Colin J. Barrow,§ Takashi Iwashita,§ Kazuo Tachibana,§ and Dinshaw J. Patel*,‡

Department of Biochemistry and Molecular Biophysics, College of Physicians and Surgeons, Columbia University, New York, New York 10032, and Suntory Institute for Bioorganic Research, Shimamoto-cho, Mishima-gun, Osaka 618, Japan

Received February 7, 1991; Revised Manuscript Received May 21, 1991

ABSTRACT: Pardaxin is a mucosal secretion of the Pacific sole *Pardachirus pavoninus* that exhibits unusual shark repellent and surfactant properties [Thompson, S. A., Tachibana, K., Nakanishi, K., & Kubota, I. (1986) *Science 233*, 341–343]. This 33 amino acid polypeptide folds into ordered structures in trifluoroethanol–water solution and in micelles but adopts a random-coiled structure in water solution. The complete proton NMR spectrum of pardaxin P-2 has been assigned in CF_3CD_2OD/H_2O (1:1) solution, and the three-dimensional structure has been elucidated with distance restrained molecular dynamics calculations. It is demonstrated that peptide segments within the 7–11 and 14–26 residue stretches are helical while residues at the C- and N-terminus exist predominantly in extended conformations in solution. The dipeptide 12–13 segment connecting the two helices exists as a bend or a hinge allowing the two helices to be oriented in a L-shaped configuration. These studies establish that pardaxin P-2 adopts a novel amphiphilic helix (7–11)–bend (12–13)–helix (14–26) motif with Pro-13 forming the focal point of the turn or bend between the two helices.

Pardaxin is a toxic material secreted by certain species of soles within the genus *Pardachirus*. It is presumably part of a defense secretion, to ward off predacious fish attacks, and its discovery resulted from attempts to isolate and identify the toxic factor secreted from the Red Sea flatfish *Pardachirus Marmoratus* (Clark, 1974), which was first reported as being an ichthyotoxic protein with a molecular weight of 17 000 (Primor, 1978). Later, the primary structure of pardaxin was determined, and its molecular weight was shown to be considerably smaller than first reported (Thompson et al., 1988).

Much attention has recently been drawn to pardaxin and other membrane active polypeptides such as gramicidin (Anderson, 1984), alamethicin (Fox & Richards, 1982), and melittin (Tosteson & Tosteson, 1982) because they serve as general models for pore-forming membrane proteins. Pardaxin has been shown to interfere with ion transport in both epithelium (Primor, 1983) and nerve cells (Renner et al., 1987). At concentrations below 10^{-7} M, pardaxin forms voltage-dependent, ion-permeable channels in artificial liposomes, whereas at somewhat higher concentrations (10^{-4}–10^{-7} M), lysis occurs (Lazarovici et al., 1986).

Our investigations on the secretion from a congeneric sole *Pardachirus pavoninus* resulted in the isolation of three ichthyotoxic and strongly surfactant peptides (Thompson et al., 1986). These peptides are nearly identical with pardaxin from *Pardachirus marmoratus* and were named pardaxin P-1, P-2, and P-3 where P refers to the species name. The amino acid sequence of pardaxin P-2 is outlined in Scheme I. They have nearly identical sequences (Thompson et al., 1986) and contain both an unusually larger number of serine residues (including a Ser-27–Ser-28–Ser-29 segment) and a large number of hydrophobic residues such as leucines and isoleucines.

Structural studies on pardaxins from *Pardachirus pavoninus* have been limited to circular dichroism (CD) measurements.

Scheme I

Amino acid sequence for Pardaxin P-2

```
                5                  10                  15
Gly-Phe-Phe-Ala-Leu-Ile-Pro-Lys-Ile-Ile-Ser-Ser-Pro-Ile-Phe-
                20                  25
Lys-Thr-Leu-Leu-Ser-Ala-Val-Gly-Ser-Ala-Leu-Ser-Ser-Ser-
30
Gly-Gly-Gln-Glu
```

These studies demonstrate that pardaxin exhibits typical α-helical CD spectra in aqueous trifluoroethanol and sodium lauryl sulfate (SDS) solutions, while it adopts a random-coiled structure in water solution. We present here a detailed high-resolution proton NMR study of pardaxin P-2 in aqueous trifluoroethanol solution. The complete spectrum has been assigned, and restrained molecular dynamic algorithms with NOE interproton data as input distance constraints have been used to determine its three-dimensional structure in solution. The major result is that the core structure of pardaxin contains a novel amphiphilic helix–bend–helix segment that distributes the polar and nonpolar residues on opposite faces of the structural motif. These studies also emphasize the importance of Pro-13 in defining the bend region between the two helical segments.

Materials and Methods

Sample Preparation. Pardaxin P-2 was synthesized in an automated fashion on a peptide synthesizer (Applied Biosystems model 430A), using the solid-phase method (Merrifield, 1963) with standard software supplied by the manufacturer.

Pardaxin P-2 was synthesized by starting from 0.5 mmol of t-Boc-Glu(OBzl)-PAM resin (600 mg) to give the resin-linked protected peptide (2.06 g) with the estimated overall yield of 53–57%. The coupling yield of each cycle, as monitored by ninhydrin coloration reaction on a several-milligram aliquot of the resin sampled after completion of each cycle, is about 97% in most cases, with some exceptional cases down to 95%. The free peptide was removed from the resin and deprotected with anhydrous hydrogen fluoride.

† This research was funded by start up funds from Columbia University to D.J.P.

* To whom correspondence should be addressed.

‡ Columbia University.

§ Suntory Institute for Bioorganic Research.

0006-2960/91/0430-8009$02.50/0

The crude peptide was purified by reverse-phase high-pressure liquid chromatography (RP-HPLC). This furnished 11.6 mg of purified pardaxin P-2 from 56 mg of the crude peptide with the following conditions: 0.05% TFA in 36–60% aqueous acetonitrile (0.45%/min gradient rate) on Cosmosil $5C_4$-300 (Nacalai tesque, Osaka) in a steel column (10 mm i.d. × 250 mm) at the flow rate of 2 mL/min, with 50 μL of 1% sample solution in 27% aqueous *n*-propanol being injected in each elution. The purified material gave a retention time on HPLC, a CD spectrum, a concentration hemolysis curve, and a ^1H NMR spectrum identical with those obtained for the natural pardaxin P-2.

A sample of pardaxin P-2 (6.0 mg, 0.0018 mmol) was prepared for NMR measurements by dissolving the sample in a 1:1 mixture (0.50 mL) of trifluoroethanol-d_3 (CD_3CD_2-OD) (Cambridge Isotopes, Inc.) and H_2O containing 25 mM potassium phosphate buffer and 0.1 mM EDTA. These conditions ensure that pardaxin adopts an ordered structure as judged by CD. The pH of the sample was adjusted to 3.5 with dilute HCl, and the final concentration of pardaxin P-2 was 3.6 mM. pH meter readings were measured at room temperature and were not corrected for isotope effects.

NMR Data Acquisition and Analyses. All proton NMR spectra were obtained at 500 MHz with a Bruker AM-500 spectrometer equipped with digital phase shifters and an Aspect 3000 computer. The data were transferred by magnetic tape to a microVAX II for processing with Dennis Hare FTNMR software. Chemical shifts are referenced to external TSP [sodium 3-trimethylsilyl(2,2,3,3-d_4)propionate]. In general, all two-dimensional NMR experiments were recorded in the phase-sensitive absorption mode with quadrature detection in both dimensions (States et al., 1982). The carrier was placed in the center of the spectrum, and a recycle delay of 1.5 s was used for all experiments. During the recycle delay and the mixing time of the NOESY experiments, the water signal was suppressed by continuous low-power irradiation from the proton decoupler channel. The spectral width was 5000 Hz in F_2, and typically 512 and 1024 increments were collected with 2048 complex data points. The time domain data sets were subsequently zero filled in F_1 to 1024 points to provide 1024 × 1024 final matrices. The base line of the rows in the final two-dimensional matrices were flattened by using a fifth-order polynomial and by manipulating the intensity of the first points in F_1 and F_2 prior to Fourier transformation (Otting et al., 1986).

Phase-sensitive NOESY spectra (Jeener et al., 1979) were acquired with mixing times of 100 and 200 ms. Double-quantum and triple-quantum filtered (DQF and TQF) COSY experiments were recorded by using 32- and 48-step phase cycling schemes as described by Morris (1986). The longer phase cycling schemes, together with narrow band frequency-rejection filters (Dykstra & Wand, 1987) that were installed at different points in the RF receiver circuitry, were helpful in reducing many artifacts originally present in these COSY experiments.

The HOHAHA experiment was run with the MLEV-17 (Bax & Davis, 1985) pulse sequence for the spin lock interval. The total MLEV-17 spin lock interval was 100 ms, and it was preceded and followed by two purge pulses of 2 ms in duration.

Molecular Dynamics Calculations. The three-dimensional structure of pardaxin P-2 in CF_3CD_2OD/H_2O (1:1) solution has been determined by application of distance restrained simulated annealing and energy minimization. Calculations were performed within the program XPLOR (Brunger 1990) using starting structures generated with random ϕ and ψ angles. Side chains were initially in an extended conformation. A total of 131 NOE-derived distance restraints were used to refine the structures. Also 22 distance restraints were used to define 11 predicted hydrogen bonds within the α-helical region (residues 14–28) (Wagner et al., 1987). Preliminary structural refinement without inclusion of the hydrogen-bond restraints had shown the predicted hydrogen bonds to be quite compatible with the experimentally observed distance restraints.

NOE cross-peak volume integrals were partitioned into three categories (strong, medium, and weak) that were converted into distance restraints (short, <2.7 Å; medium, <3.3 Å; and long, <5.0 Å). Appropriate restraint corrections were made for those restraints involving methyl groups, aromatic $^\delta$CH and $^\epsilon$CH protons, and chemical shift degenerate methylene protons (Wuthrich et al., 1982) to allow center averaging of the restraints. Specific restraints at prochiral centers and aromatic $^\delta$CH and $^\epsilon$CH protons were included only for those protons showing consistent positional preference during preliminary structural calculations.

Simulated annealing was carried out according to the YASAP protocol (Brunger, 1990) with 24 ps of 1000 K annealing during which the forces due to the distance restraints and atomic size were kept very small for the first 15 ps and then increased during the last 9 ps. Cooling to a final 300 K was accomplished over a period of 2.52 ps with the distance restraint force set to 50 kcal A^{-2}.

Structure calculations were repeated 50 times with different random starting conformations. The number of accepted final structures was reduced to 33 by discarding those that displayed total energies greater than 222 kcal mol^{-1}. Structures that at this stage exhibited total energies greater than 222 kcal mol^{-1} had been observed to contain unacceptable restraint violations. The accepted structures were energy minimized by using a full force field (CHARMM) and constant dielectric 80. During the minimization computations the distance restraint force was set to 10 Kcal A^{-2}.

Results

Spin-System Identification. The one-dimensional proton NMR spectrum of pardaxin P-2 (3.6 mM) obtained in CF_3CD_2OD/H_2O (1:1) at pH 3.5 and 40 °C is plotted in Figure S1A (supplementary material). A one-dimensional NMR spectrum obtained with 0.36 mM pardaxin P-2 was virtually identical with that obtained at 3.6 mM, thus demonstrating that the structure of pardaxin is monomeric within the concentration range. The H_2O signal was suppressed by selective presaturation (2 mW) for 1.5 s prior to data acquisition. Despite the 33% volume of deuterium relative to protium in the solvent mixture, the amide (NH) resonances are clearly visible in the downfield region with lower intensity than the remaining protons due to exchange with deuterium. Nevertheless, we were able to unambiguously assign all of the amide resonances to a particular amino acid. Expanded plots of the amide region at 40 and 30 °C are shown in Figures S1B and S1C.

Pardaxins contain a large number of serines, leucines, and isoleucines (Scheme I) leading to considerable overlap of resonances in the COSY spectra. However, by using multiple quantum filtered techniques, we were able to remove much of the ambiguity due to overlap especially in the crowded upfield aliphatic region where the 16 methyls of both the leucines and isoleucines lie within a 1 ppm region.

Figure 1A shows how the A_3MP spin systems for the $^\delta CH_3$ and $^\gamma CH_2$ of the four isoleucines can be easily located in the TQF-COSY experiment. The $^\alpha$CH and $^\gamma CH_2$ resonances can

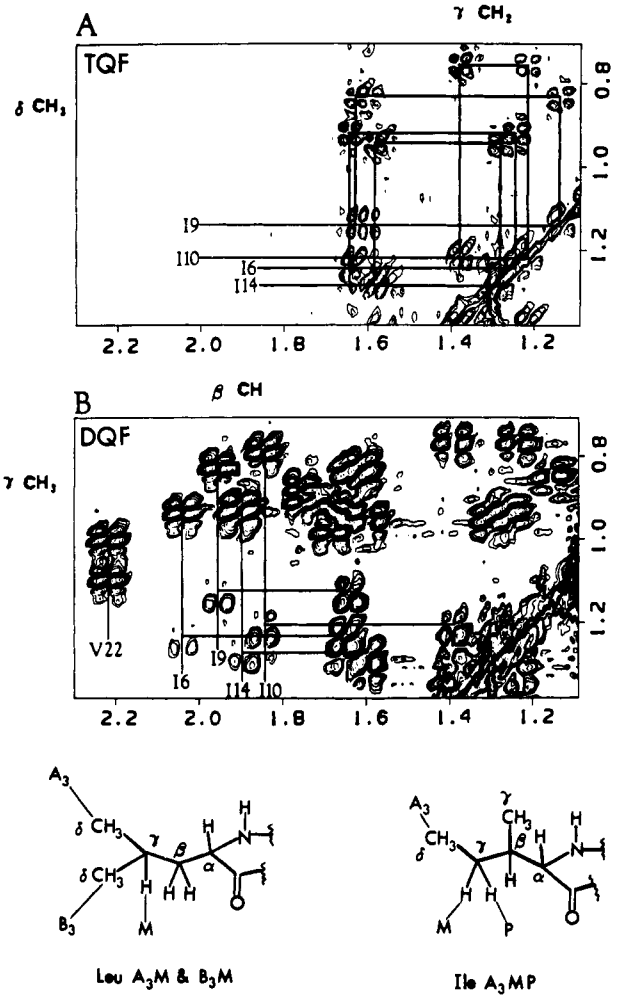

FIGURE 1: Identification of aliphatic methyl and methylene peaks with (A) triple-quantum filtered (TQF) COSY and (B) double-quantum filtered (DQF) COSY experiments. In the top trace, the $^{\delta}CH_3$–$^{\gamma}CH_2$ cross peaks for the four isoleucines are identified since the two γ methylene protons are nonequivalent (A_3MP spin systems) and thus not removed by a TQF. Further connections of the methylene protons in the DQF-COSY allowed assignments of the β methine and γ methyl peaks of the isoleucines. The assignments for Val-22 are also shown.

then be connected to the remaining $^{\beta}CH$ and $^{\gamma}CH_3$ resonances of the isoleucines in DQF-COSY data (Figure 1B). Cross peaks for the methyls of the leucines are not detected in the TQF-COSY data since the methyls are part of A_3M and B_3M (two-spin) systems. In contrast, the A_3MP spin systems of the isoleucines is a three-spin system and therefore is detectable in a TQF-COSY experiment. The valine peaks are also identified in Figure 1B as evidenced by the small chemical shift difference between the two methyl groups, their lower field position relative to the other methyl groups of the isoleucines and the leucines, and their identical vicinal coupling to the adjacent proton.

The $^{\alpha}CH$ cross peaks for the aliphatic amino acid residues were identified from relay patterns obtained in the HOHAHA spectra and then confirmed from DQF-COSY data that displays only three bond vicinal $^{\beta}CH$ and $^{\gamma}CH$ couplings. The $^{\alpha}CH$ protons for the four isoleucines and the valine were easily identified from strong relay patterns seen from the methyl protons. This is shown in Figure S2 (supplementary material) where data from the HOHAHA and DQF-COSY are superimposed. Once the isoleucine and valine relay peaks were identified, the remaining δ relay peaks were, on the basis of elimination, presumed to be leucine δ methyl to $^{\alpha}CH$ relays.

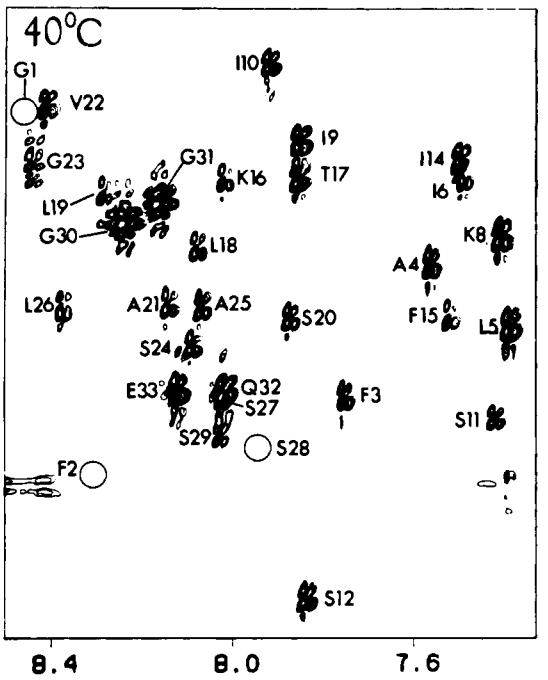

FIGURE 2: DQF-COSY spectra containing $^{\alpha}CH$–NH cross peaks (fingerprint region) of pardaxin P-2 at 40 °C. Sequence-specific assignments of the peaks are as indicated. Cross peaks too weak to observe at the contour level plotted or those saturated by the decoupler are indicated by circles.

Additionally, two DQF-COSY cross peaks for the $^{\beta}CH_2$ to $^{\alpha}CH$ couplings were seen for each of the remaining relay peaks thus confirming the assignment of these peaks as leucines.

The three alanine and one threonine residues were identified by the intense DQF-COSY cross peaks in the $^{\alpha}CH$ region (Figure S2); i.e., the only methyl to methine couplings in the low-field region. Identification of the two lysine and the two proline spin networks were made on the basis of long-range relays from the $^{\epsilon}CH_2$ to $^{\alpha}CH$ and $^{\delta}CH_2$ to $^{\alpha}CH$, respectively.

The two AMPTX spin systems of Gln-32 and Glu-33 were located by using HOHAHA and DQF-COSY data (Figure S2). Two of the three phenylalanine AMX spin systems were apparent in DQF-COSY data recorded at 40 °C. The remaining phenylalanine AMX cross peaks appeared in DQF-COSY data recorded at 30 °C, since at 40 °C the $^{\alpha}CH$ peak resided under the H_2O signal and was bleached out by the irradiation of the proton decoupler. The remaining seven serine and four glycine (AMX and AX) spin systems were tentatively located by their low-field positions (all resonances appear downfield of 3.8 ppm) and later confirmed from sequential assignments by using the labile NH protons.

Sequential Assignments. Sequence-specific resonance assignments were made by using through-space sequential NOE connectivities between $^{\alpha}CH$ and $^{\beta}CH$ with the NH (amide) protons ($d_{\alpha N}$, $d_{\beta N}$, and d_{NN}). The fingerprint region of the DQF-COSY spectrum for data collected at 40 °C is shown in Figure 2. Each cross peak is sequence specifically labeled. The cross peaks for Phe-2 and Ser-28 are absent in the 40 °C data due to saturation from the irradiation of the water line. However, these cross peaks appeared in the 30 °C data. Attempts at estimating $^3J(NH-^{\alpha}CH)$ coupling constants from DQF-COSY data gave values in the range of 7–10 Hz. Thus, despite the low pH of the solution (pH 3.5) and elevated temperatures, the line widths of the NH resonances are too broad to permit accurate measurements of coupling constant data. A similar situation occurred for NMR studies of secretin in trifluoroethanol–water mixtures (Gronenborn et al., 1987).

Table I: Pardaxin P-2 ^{1}H NMR Resonance Assignments at 40 °C in CF_3CD_2OD/H_2O (1:1), pH 3.5[a]

residue	NH	$^{\alpha}$CH	$^{\beta}$CH	others
G-1	8.45	3.88, 3.81		
F-2	8.33	4.61	3.09, 3.08	2,6H, 7.16; 3,5H, 7.31; 4H, 7.39
F-3	7.75	4.48	3.15, 3.06	2,6H, 7.25; 3,5H, 7.39; 4H, 7.39
A-4	7.57	4.18	1.41	
L-5	7.38	4.33	1.89, 1.65	$^{\gamma}$CH, 1.72; $^{\delta}CH_3$, 0.98; $^{\delta}CH_3$, 0.92
I-6	7.49	3.99	2.02	$^{\gamma}CH_3$, 0.93; $^{\gamma}CH_2$, 1.64, 1.26; $^{\delta}CH_3$, 0.92
P-7		4.26	2.35, 1.85	$^{\gamma}CH_2$, 2.13, 1.94; $^{\delta}CH_2$, 3.68, 3.68
K-8	7.41	4.11	2.01, 1.96	$^{\gamma}CH_2$, 1.58, 1.51; $^{\delta}CH_2$, 1.74, 1.74; $^{\epsilon}CH_2$, 3.02, 3.02
I-9	7.85	3.91	1.95	$^{\gamma}CH_3$, 0.82; $^{\gamma}CH_2$, 1.63, 1.14; $^{\delta}CH_3$, 0.84
I-10	7.91	3.73	1.84	$^{\gamma}CH_3$, 0.78; $^{\gamma}CH_2$, 1.38, 1.22; $^{\delta}CH_3$, 0.77
S-11	7.42	4.52	4.13, 3.99	
S-12	7.83	4.92	4.32, 4.32	
P-13		4.25	2.35, 1.85	$^{\gamma}CH_2$, 2.13, 1.94; $^{\delta}CH_2$, 3.68, 3.68
I-14	7.50	3.95	1.88	$^{\gamma}CH_3$, 0.92; $^{\gamma}CH_2$, 1.58, 1.29; $^{\delta}CH_3$, 0.94
F-15	7.52	4.29	3.31, 3.30	2,6H, 7.26; 3,5H, 7.31; 4H, 7.39
K-16	8.02	3.98	2.00, 200	$^{\gamma}CH_2$, 1.56, 1.56; $^{\delta}CH_2$, 1.78, 1.78; $^{\epsilon}CH_2$; 3.07, 3.07
T-17	7.83	3.98	4.42	$^{\gamma}CH_3$, 1.30
L-18	8.07	4.15	1.78, 1.68	$^{\gamma}$CH, 1.74; $^{\delta}CH_3$, 0.91; $^{\delta}CH_3$, 0.88
L-19	8.28	4.03	1.62, 1.52	$^{\gamma}$CH, 1.58; $^{\delta}CH_3$, 0.84; $^{\delta}CH_3$, 0.83
S-20	7.87	4.30	4.16, 4.02	
A-21	8.13	4.27	1.61	
V-22	8.40	3.83	2.22	$^{\gamma}CH_3$, 1.10, 1.00
G-23	8.43	3.97, 3.86		
S-24	8.04	4.36	4.12, 4.04	
A-25	8.06	4.28	1.60	
L-26	8.36	4.27	1.93, 1.86	$^{\gamma}$CH, 1.31; $^{\delta}CH_3$, 0.95; $^{\delta}CH_3$, 0.94
S-27	8.01	4.47	4.11, 4.05	
S-28	7.95	4.56	4.11, 4.06	
S-29	8.03	4.56	4.09, 4.04	
G-30	8.22	4.07, 4.07		
G-31	8.15	4.06, 4.00		
Q-32	8.02	4.47	2.21, 2.06	$^{\gamma}CH_2$, 2.43, 2.43; $^{\epsilon}NH_2$, 7.38, 6.62
E-33	8.12	4.45	2.24, 2.07	$^{\gamma}CH_2$, 2.52, 2.52

[a] Concentration of Pardaxin P-2 was 3.6 mM. The solvent mixture contained 25 mM potassium phosphate buffer and 0.1 mM Na_2EDTA. Chemical shifts are referenced to internal TSP and are reported in ppm.

Many of the NH assignments were confirmed from relay patterns observed in the HOHAHA spectrum. In particular, as shown in Figure S3A (supplementary material), the NH–$^{\alpha}$CH–$^{\beta}CH_2$ relay system of the serines was useful since many of the $^{\alpha}$CH–$^{\beta}CH_2$ peaks were bleached by the H_2O signal trail in the DQF-COSY spectrum. All three phenylalanine residues displayed similar four bond relays, including Phe-2, which was especially helpful since the $^{\alpha}$CH peak is missing due to bleaching of the H_2O resonance.

Using the NOESY spectrum, it was possible to trace a path of sequential NHs along the backbone from Lys-8 to Ile-9, Ile-10 to Ser-12, Ile-14 to Lys-16, and Thr-17 to Ser-27 (Figure 3). The connectivity is lost between Lys-16 and Thr-17 although at lower temperature (30 °C) a weak NOE was seen between these two residues. In addition, several $^{\alpha}CH_i$–NH_{i+1} connectivities were observed and are shown in Figure S4 (supplementary material).

No differences in NOEs were observed between 30 and 40 °C, suggesting that there are no structural changes occurring between these two temperatures. There were a few exceptions in the $d_{\alpha N}$ NOEs for residues 27–33 (Figure S4), which were much weaker in the 40 °C data (Figure S4B) and may be due to the increased mobility of the C-terminal end of the peptide. Most of the interresidue NOEs in the fingerprint region are $d_{\alpha N}$ connectivities, although a few $d_{N\alpha}$ (in the opposite sense) were also observed. Cross peaks for $d_{\beta N}$ and $d_{N\delta}$ connections to Pro-7 and Pro-13 were seen (Figure S5, supplementary material). Other interresidue NOEs in the fingerprint region and among the $^{\beta}CH_2$, $^{\gamma}CH_2$, $^{\gamma}CH_3$, and NH protons are summarized in an expanded NOESY plot (Figure S6, supplementary material).

A summary of the sequential NOEs of pardaxin P-2 are shown in Figure 4. Table I contains the complete ^{1}H NMR assignments of pardaxin P-2 at 40 °C.

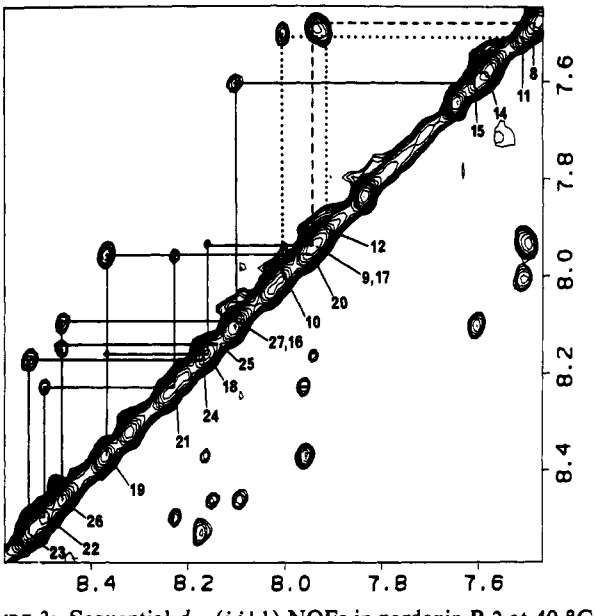

FIGURE 3: Sequential $d_{NN}(i,i+1)$ NOEs in pardaxin P-2 at 40 °C. Solid, dashed, and dotted lines follow connectivities in different parts of the molecule with the amide resonances labeled at the diagonal.

Distance Connectivities between Nonadjacent Residues. There are two types of interresidue NOEs observed between the labile NH protons and other nonlabile protons. Both types of interactions are tabulated separately in Figures 4A and 4B, and both interactions are representative for interproton contacts between residues as one proceeds from the N- to the C-terminus. For example, the $^{\alpha}CH_i$–NH_{i+4} NOE seen between Lys-8 and Ser-12 exemplifies an interaction between

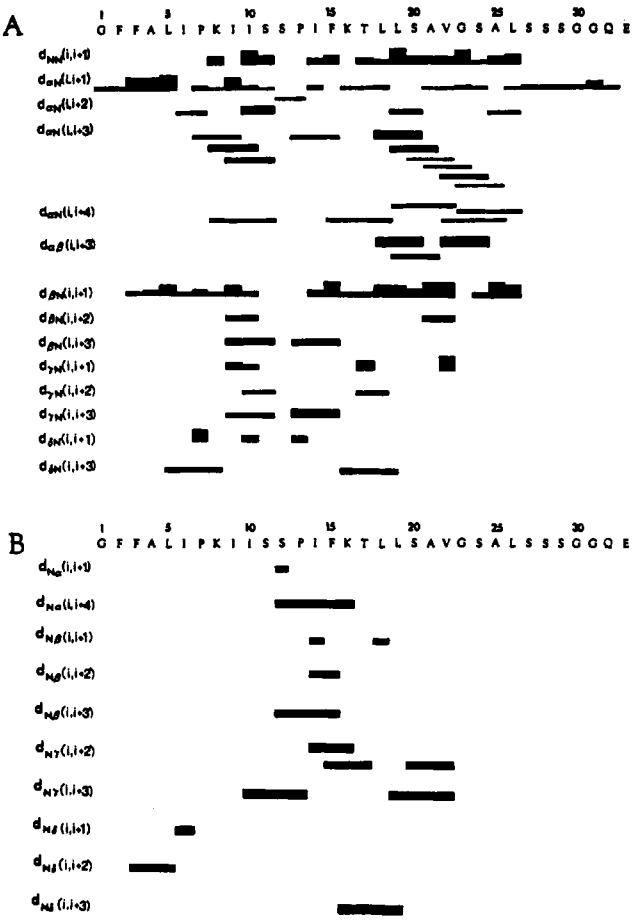

FIGURE 4: Summary of the interresidue NOE connectivities involving the NH, $^{\alpha}$CH, $^{\beta}$CH, $^{\gamma}$CH, and $^{\delta}$CH protons. The NOEs are classified into strong, medium, and weak according to the thickness of the bar heights. Shown is a combination of data acquired at 30 and 40 °C (see text). In the upper trace (A) most NOE contacts (except d_{NN} NOEs) represent through-space contacts between a nonlabile proton with an amide (NH) proton. The NOEs listed in the lower trace (B) also represent interproton contacts between residues proceeding toward the C-terminus, but now the proton assignments are reversed.

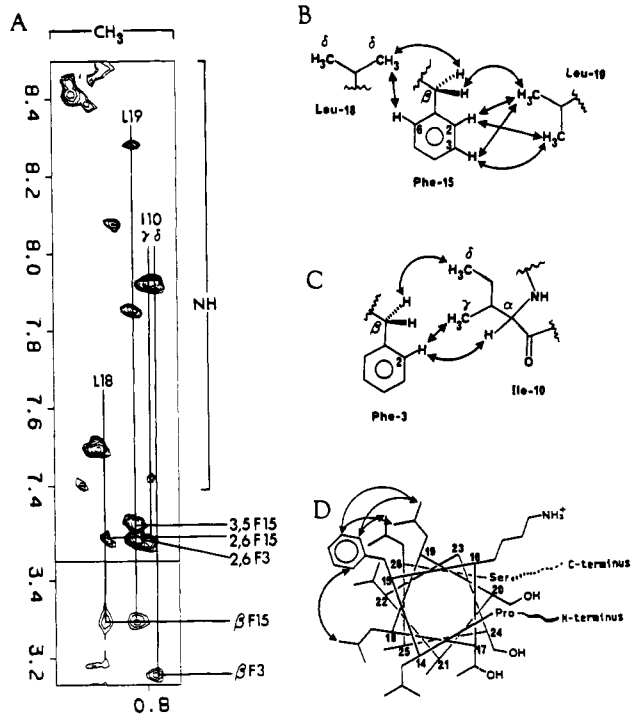

FIGURE 5: (A) Expanded region of 200-ms mixing time NOESY obtained at 40 °C. This region demonstrates close contacts between (B) the methyls of Leu-18 and Leu-19 to protons of Phe-15 and (C) close contacts between Phe-3 and Ile-10. An axial or helical wheel projection of the helix formed between residues 13 and 27 is shown with arrows representing NOE contacts from Phe-15 to Leu-18 and Leu-19. This projection illustrates the amphiphilic nature of the helix.

the $^{\alpha}$CH of Lys-8 and the NH of Ser-12. This contact is listed in Figure 4A and is a typical NOE seen in proteins (Wuthrich, 1986). Additional NOEs, however, were seen between the same types of protons only now in the opposite sense, and these NOEs are summarized in Figure 4B. For example, the NH of Ser-12 displays NOEs to three nonexchangeable protons of residues located further along the polypeptide chain toward the C-terminus: NH_i–$^{\alpha}CH_{i+1}$, NH_i–$^{\alpha}CH_{i+4}$, and NH_i–$^{\beta}CH_{i+3}$. These latter interactions represent contacts between the NH of Ser-12 and the $^{\alpha}$CH of Pro-13, the $^{\alpha}$CH of Lys-16, and the $^{\beta}CH_2$ of Phe-15, respectively. Interestingly, most of these "opposite" direction NOEs (Figure 4B) are centered within the Ser-12 to Lys-16 segment, which as later deduced from the molecular dynamics calculations indicate that a bend or turn along the main chain occurs within this region. Some additional NOEs include $d_{N\delta}$ interactions between Leu-5 and Ile-6, Phe-3 and Leu-5, and Phe-15 and Leu-18 (Figure 4B) were also present and are interesting since they represent contacts between polar NH proton and nonpolar side-chain protons. This may be due to strong hydrogen bonding of the NH protons and their being packed inside a hydrophobic patch of aliphatic side chains. Similar NOEs were seen in the opposite sense (Figure 4A). For instance, a $^{\delta}CH_3$ of Leu-5 displays an NOE to the NH of Lys-8, and the $^{\delta}CH_2$ of Lys-16 has a NOE to the NH of Leu-19. These are listed as $^{\delta}CH_i$–NH_{i+3} NOEs in Figure 4A. All of the NOEs are assigned in expanded NOESY plots (Figure S6, supplementary material).

Both of the X–Pro peptide bonds between residue 6–7 and 12–13 are presumably trans in configuration due to the lack of $^{\alpha}$CH(X) to $^{\alpha}$CH(Pro) NOEs and the presence of strong NH(X) to $^{\alpha}CH_2$(Pro) NOEs. Sequential assignments of the next residues (Lys-8 and Ile-14) were made with $^{\delta}CH_{2i}$ to NH_{i+1} NOEs.

Additional interresidue NOEs among several hydrophobic residues were also detected in both short (100 ms) and long (200 ms) mixing time NOESY data. These NOEs are shown in Figure 5 where arrows are representative for the observed NOEs. Previous calculations (Thompson et al., 1987) based on CD data predicted that an α-helical region resides between Pro-13 and Ser-27. The backbone NOE patterns (Figure 6) and side-chain NOEs (Figure 5) in the present NMR study also indicate that an α-helix is present in this region. An axial projection of residues 13–27 is shown in Figure 5D. In this model, the polypeptide chain is amphiphilic with the hydrophobic and hydrophilic residues oriented on opposite sides of the helix. Our NOE data provide evidence supporting this model. For example, interproton NOEs observed from Leu-18 and Leu-19 to Phe-15 (Figure 5B) are indicated with arrows (Figure 5D). Other contacts between Phe-3 and Ile-10 are shown in Figure 5C. These latter connections were the only NOEs seen between amino acids separated by more than four residues and may indicate that some tertiary folding of pardaxin occurs near the N-terminus.

Molecular Dynamics Calculations. The protocol for the structural refinement has been outlined under Material and Methods. The 33 structures derived from simulated annealing and distance restrained energy minimization exhibit structural convergence within residues 6–26 (backbone in Figure 6A,

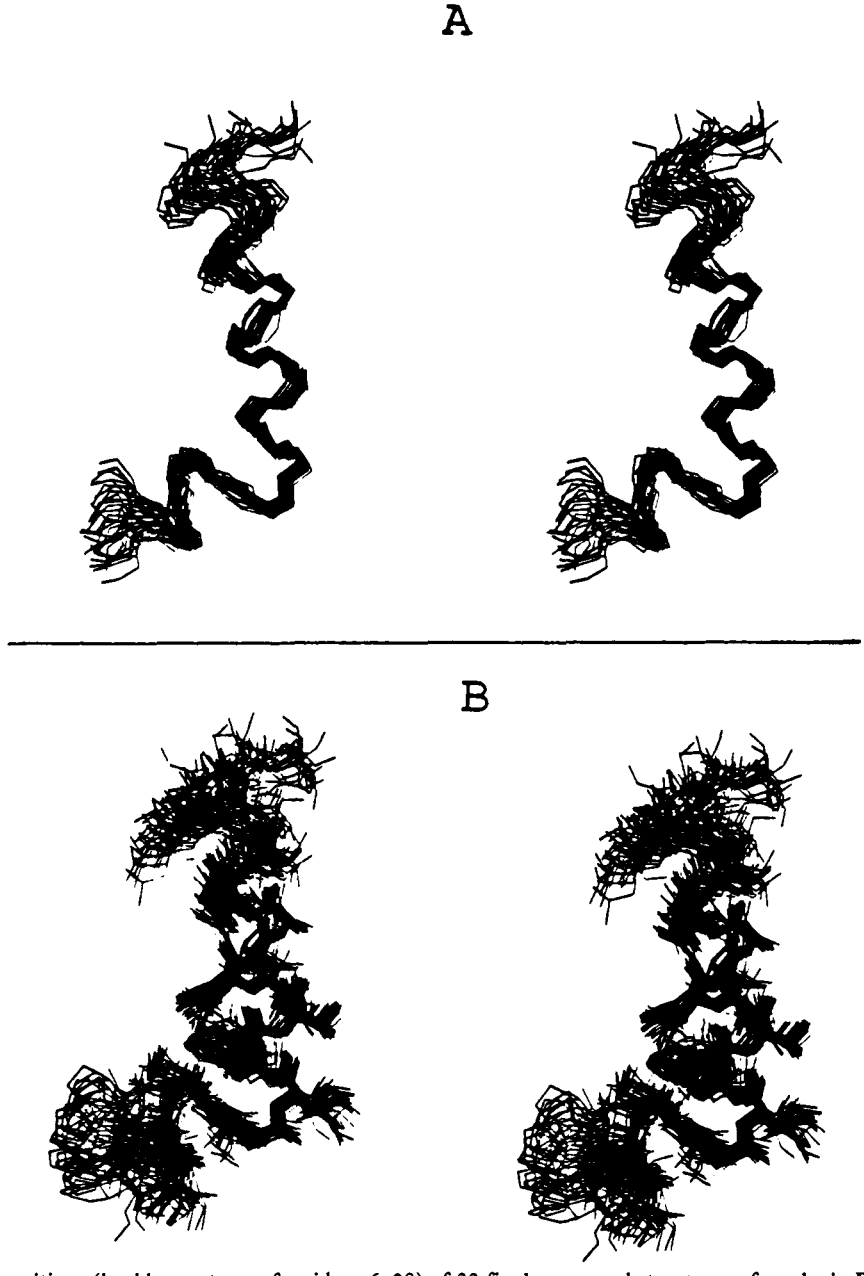

FIGURE 6: Best-fit superpositions (backbone atoms of residues 6–28) of 33 final converged structures of pardaxin P-2, defined from random backbone angle starting structures. Figures show cross-eyed stereoview of (A) C^{α}, C, and N atoms of residues 3–28; (B) all non-hydrogen atoms of residues 3–28.

Table II: The Mean, Standard Deviation, Minimum, and Maximum Values for 33 Final Refined Structures of Pardaxin P-2

	tot[a]	NOE[b]	vdw[c]	angle[d]	dihed[e]	elect[f]	impr[g]	rmsd[h]
mean	204.7	30.45	-92.0	92.1	182.8	-5.3	2.2	0.1541
SD	14.5	2.79	4.17	4.08	13.22	0.52	0.35	0.0071
min	158.3	25.3	-99.2	85.8	149.5	-6.4	1.5	0.1410
max	242.5	36.4	-83.2	101.0	218.6	-4.2	2.9	0.1690

[a] Total potential energy (kcal mol^{-1}). [b] Potential energy (kcal mol^{-1}) due to distance restraint violations, with a square-well potential and force constant set at 10 kcal A^{-2}. [c] Potential energy (kcal mol^{-1}) due to van der Waals interactions. [d] Potential energy (kcal mol^{-1}) due to angle strain (bending). [e] Potential energy (kcal mol^{-1}) due to local 3-bond interactions. [f] Electrostatic potential energy (kcal mol^{-1}) calculated with a constant dielectric of 80. [g] Potential energy (kcal mol^{-1}) due to improper terms that serve to maintain planarity. [h] Root-mean-square deviation of distance restraints.

backbone and side chains in Figure 6B) and a mean RMSD for distance restraint violations of 0.154 Å with a range of ±0.014 Å. The experimental distance restraints (Figure 7A) and the coordinate RMSD per residue (Figure 7B) show an inverse correlation. Residues 1–6 and 27–33 are poorly defined by experimental restraints (Figure 7A), and this is reflected in the high coordinate RMSD per residue (Figure 7B) and apparent disorder seen in the overlaid structures (backbone in Figure S7, supplementary material). The potential energies of the final energy minimized structures are of reasonable magnitude and exhibit small structure to structure deviations (Table II). The small values seen for the electrostatic potential energies is simply a reflection of the fact that within the simulated annealing protocol the electrostatic term is not included

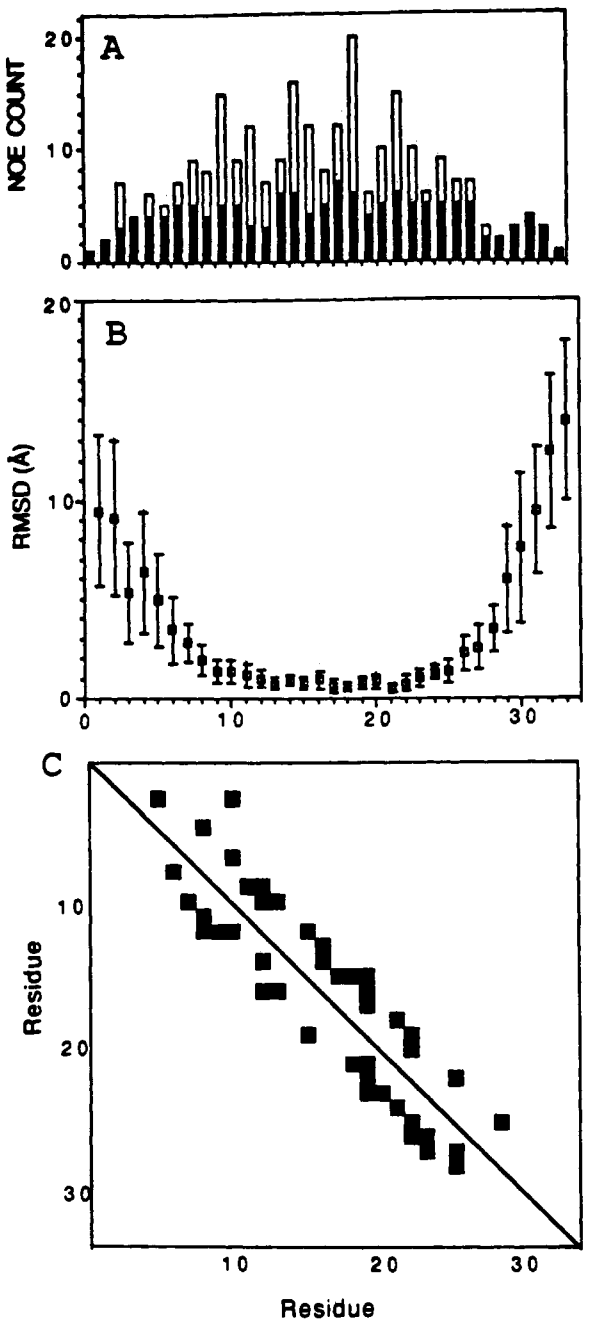

FIGURE 7: Distance restraint and coordinate root-mean-square difference distribution throughout the 33 refined pardaxin P-2 structures. (A) Distribution of sequential (i to i+1) distance restraints (filled columns) and longer range (greater than i to i+1) distance restraints (open columns). (B) Root-mean-square coordinate difference (backbone atoms only) per residue with standard deviations shown as error bars. (C) Distribution of distance restraint connectivities. Filled squares represent one or more restraints between residues located on the diagonal. Below the diagonal are restraints between $^{\alpha}$CH and NH protons only. Above the diagonal are restraints involving at least one side-chain proton.

in the global potential, and also that a constant dielectric of 80 was used for the final restrained energy minimization. The distribution and conformation of the charged or polar side chains is of particular interest in this protein and because of this it is important that any apparent conformation preference amongst the structures be a consequence only of the experimental restraints and steric interactions.

Discussion

The NMR data for pardaxin P-2 clearly demonstrates that the polypeptide assumes a well-ordered three-dimensional structure in trifluoroethanol–water solution. Both the N- and C-terminal ends are ill-defined by experimental distance restraints and exhibit a high degree of disorder in the refined structures. Overall, the pattern of NOEs and the results of the structural determinations indicate that pardaxin P-2 is composed of five structurally distinct peptide segments: 1–5, 6–11, 12–13, 14–26, and 27–33. Residues located at the C-terminal end of the protein (27–33) appear to exist in an extended conformation; the N-terminal residues have some long-range interactions (Figure S7) and some ordering of the spatial arrangement of the side chains, even though the coordinate RMSD is quite large. The region between residues 14 and 26 is α-helical (Figure 6) with low coordinate RMSD in both backbone and side-chain atoms. Residues 6–12 form a right-handed helix of relatively poor definition, especially with regards to the side chains. There is insufficient data to be precise as to the character of this helical region. The region about residues 12 and 13 exists as a bend or hinge creating an angle of almost 90° between the two helical segments.

Secondary Structure Determination from Analysis of NOESY Data. The NOE data summarized for pardaxin P-2 in Figure 4 clearly reveal a distinct helical region extending from residues 14 to 26, being characterized by stretch of NH_i–NH_{i+1} NOEs and the presence of $^{\alpha}CH_i$–NH_{i+3} and $^{\alpha}CH_i$–$^{\beta}CH_{i+3}$ NOEs. As mentioned before, the NH_i–NH_{i+1} connectivity is lost between Lys-16 and Thr-17, although at lower temperatures (30 °C) a weak NOE was seen between these two residues. The intensity of the NOEs throughout this region is irregular as well as the lack of some $^{\alpha}CH_i$–NH_{i+3} NOEs from residues 14–18 and residues 24–26. However, the long stretch of $^{\beta}CH_i$–NH_{i+1} NOEs together with the NH_i–NH_{i+1} NOEs is strongly indicative of a helix. This closed loop pattern of NH_i to NH_{i+1} and $^{\beta}CH_i$ to NH_{i+1} NOEs is typical for helices (Di Stefano & Wand, 1987). The regions within residues 7–11, however, display an NOE pattern typical of turns, although the presence of both $^{\alpha}CH_i$–NH_{i+3} and $^{\alpha}CH_i$–NH_{i+4} NOEs suggests that a second helix exists within this region. The peptide segments between residues 1–6 and 27–33 have the characteristics of an extended conformation exemplified by the stretch of $^{\alpha}CH_i$–NH_{i+1} NOEs and the absence of other short-range NOEs involving the NH and $^{\alpha}$CH protons.

Three-Dimensional Structural Determination. The results of the restrained simulated annealing and energy minimization demonstrate convergence to a single family of structures (Figure 6). All 33 final structures show acceptable error with regards to experimentally measured distances and reasonable potential energies (Table II). Between resides 6 and 28 the RMS coordinate deviation is less than 0.4 Å per residue, although the rest of the protein is less well defined (Figure S7). There is no evidence that either of the terminal regions fold back on the rest of the molecule, so that the overall structure is extended and nonglobular. The three-dimensional structure is defined by a helix–bend–helix segment spanning residues 6–28 with the bend centered at residues 12 and 13. Thus pardaxin P-2 adopts an L-shaped global conformation in structure-forming solvents. It is clear that the bend is associated with Pro-13, which effectively facilitates a half-turn unwinding, and a 90° bend between the two helical segments. This allows both amphiphilic helical segments to present their polar residues on one common face.

Helix–Bend–Helix Motif. The peptide segments within residues 7–11 and 14–26 adopt helical structures as judged from analysis of the NMR data and the structures obtained from the molecular dynamics refinements. The α-helical

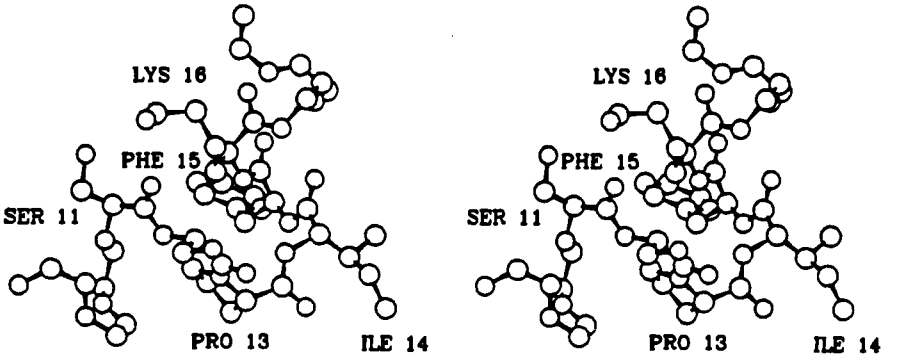

FIGURE 8: Ball and stick diagram of a representative "bend region" structure. Cross-eyed stereoviews showing residues 8–19 are shown as backbone atoms only. Residues 11–16 are shown as all non-hydrogen atoms.

stretch between residues 14 and 26 is closer to ideality and is clearly amphiphilic in nature. In fact, the tendency of small polypeptides to form amphiphilic α-helices is a quite general feature (Kaiser & Kezdy, 1987); i.e., apolipoprotein (Fukushima et al., 1979), alamethicin (Fox & Richards, 1983), melittin (DeGrado et al., 1981), δ-hemolysin (Tappin et al., 1988), and cecropin A (Holak et al., 1988). In the helical wheel projection for residues 14–26 (Figure 5D), the nonpolar residues (Ile-14, Phe-15, Leu-18, Leu-19, Ala-21, Val-22, Ala-25, and Leu-26) reside on an opposite face with respect to the more polar or charged residues (Lys-16, Thr-17, Ser-20, and Ser-24). This amphiphilic alignment within the helix probably accounts for part of the highly surfactant nature of the pardaxins.

The peptide segment within the 7–11 region appears to be a somewhat more distorted helix. The long-range NOE contacts between Phe-3 and Ile-10 (Figure 5C) probably accounts to some extent for this distortion although closer examination of the types of residues within this helical segment may also offer some explanation. Thus, none of the residues within this stretch are compatible with the formation of a stable α-helical motif (Schulz & Schirmer, 1979). Also, the lack of a hydrogen-bond donor from Pro-7 causes the helix to be unfavorably aligned. Nonetheless, the 7–11 segment, is amphiphilic.

An expanded picture of the bend between the two helices is shown in Figure 8. Clearly, Pro-13 is a pivot in this region and initiates the helix found within residues 14–26. This is a common feature of prolines in membrane proteins as they are conformationally restricted and adopt the proper dihedral angles needed for helix initiation. It appears possible that the bend is stabilized by formation of a hydrogen bond from the terminal NH_3^+ of Lys-16 to the carbonyl oxygen of Ser-11. The location of the Lys-16 side chain within the interior of the bend region is readily defined and explicable by numerous NOEs from the backbone amide protons of Ser-12 and Ile-14 (Figure 4B). Thus, the NH of Ser-12 makes close contact with the $^{\alpha}CH$ of Lys-16 and the NH of Ile-14 shows NOE contacts to the β and γ methylene protons of Lys-16. With the exception of a weak NOE contact between the $^{\alpha}CH$ of Ser-12 and the NH of Ile-14 (Figure 4A), no other interresidue NOEs from the $^{\alpha}CH$ and $^{\beta}CH_2$ of Ser-12 were detected. This is readily explained by Ser-12 $^{\beta}CH_2OH$ being solvent exposed as depicted in Figure 8.

Other transmembrane polypeptides that also form voltage-gated ion channels appear to contain hinge regions near the center of the molecules. Melittin adopts an α-helical conformation along its length in both the crystalline state (Terwilliger & Eisenberg, 1982) and in methanol solution (Bazzo et al., 1987) with a hinge between residues 11 and 12 situated in the center of the helix. This distortion of the helix was primarily due to the absence of a hydrogen bond to the carbonyl oxygen of Thr-10 from Pro-14 since prolines lack an amide proton. The longer 33 amino acid polypeptide pardaxin has a more pronounced bend between its helical segments with Pro-13 playing a critical role in defining the bend. Indeed, the helix–helix angle formed between segments 7–11 and 14–26 is approximately 90° in pardaxin P-2 compared to 20° for melittin as determined in methanol solution (Bazzo et al., 1987). It should be noted, however, that there is little difference in the end-to-end distances between the folded conformations of melittin and pardaxin. In addition, the bend centered at residues 12–13 in pardaxin P-2 allows the polar residues (Lys-8, Lys-16, Ser-11, Ser-12, and Thr-17) to reside on one face of the molecule. By contrast, if pardaxin were fully helical, the nonterminal polar residues in the helical segment would no longer be distributed on one face of the helix.

Pore Formation. The lytic and shark repellent activities of the pardaxins have been attributed to their interference with ion transport (Primor, 1983). In aqueous solution pardaxin exists as a tetramer, but it spontaneously assembles in membranes to form voltage-gated ion channels or pores. This process is undoubtedly closely related to the means by which other water-soluble toxins (such as melittin) spontaneously assemble in membranes (Knoppel et al., 1979).

The L-shaped structure of pardaxin P-2 obtained in the present study permits us to propose a model for the interaction of pardaxin with membranes to generate a pore. NOESY and COSY spectra for pardaxin P-1, which contains Leu instead of Ile at position 14 and, Glu instead of Gly at position 3, suggest an almost identical secondary structure with that of pardaxin P-2. Observed variations in pardaxin sequences appear to be structurally unimportant. This suggests that the results given here for protein pardaxin P-2 are probably general for all pardaxins. While our structure was determined in trifluoroethanol–water solution rather than in a more realistic biological membrane environment, other membrane proteins have been shown to adopt similar conformations in trifluoroethanol–water mixtures and in dodecylphosphocholine micelles (Braun et al., 1983; Clore et al., 1986b). This suggests that trifluoroethanol, by reducing water activity and strengthening hydrogen bonds, may be suitable for modeling the pardaxin conformation at a lipid bilayer. Nevertheless, some details of the structure may be influenced by the properties of the membrane, and work is currently in progress to investigate these possibilities.

ACKNOWLEDGMENTS

We thank Dr. Stewart Thompson for helpful discussions and Dr. Koji Nakanishi (director of SUNBOR) for support and

encouragement. The NMR spectrometers were purchased from funds donated by the Robert Woods Johnson Jr. Trust and Matheson Trust toward setting up an NMR Center in the Basic Medical Sciences at Columbia University.

Supplementary Material Available

Figures S1 to S7, showing one-dimensional NMR spectra of pardaxin in CF_3CD_2OD/H_2O (1:1), pH 3.5 at 30 and 40 °C (Figure S1); superimposed HOHAHA and DQ-COSY spectra (Figure S2); HOHAHA spectrum establishing relayed connectivities representing NH–$^{\alpha}$CH–$^{\beta}CH_2$ (Figure S3); sequential $d_{\alpha N}(i,i+1)$ in NOESY and DQ-COSY spectra (Figure S4); $d_{\alpha N}$ and $d_{N\alpha}$ NOEs in pardaxin (Figure S5); $d_{\beta N}$, $d_{\alpha N}$, and $d_{\delta N}$ NOEs as well as $d_{N\beta}$, $d_{N\alpha}$, and $d_{N\delta}$ NOEs in pardaxin (Figure S6); and best-fit superpositions (backbone atoms) of 33 final converged structures of pardaxin P-2 (Figure S7) (9 pages). Ordering information is given on any current masthead page.

Registry No. Pardaxin P-2, 104883-59-2; Pro, 147-85-3.

References

Anderson, O. A. (1984) *Annu. Rev. Physiol. 46*, 531–548.

Bax, A., & Davis, D. G. (1985) *J. Magn. Reson. 65*, 355–360.

Bazzo, R., Tappin, M. J., Pastore, A., Harvey, T. S., Carver, J. A., & Campbell, I. D. (1988) *Eur. J. Biochem. 173*, 139–146.

Braun, W., Wider, G., Lee, K. H., & Wuthrich, K. (1983) *J. Mol. Biol. 191*, 553–561.

Brooks, B. R., Bruccoleri, R. E., Olafson, B. D., States, D. J., Swaminathan, S., & Karplus, M. (1983) *J. Comput. Chem. 4*, 187–217.

Brunger, A. (1990) XPLOR manual V2.2, Yale University.

Clark, E. (1974) *Natl. Geogr. 146*, 719.

Clore, G. M., Brunger, A., Karplus, M., & Gronenborn, A. M. (1986a) *J. Mol. Biol. 191*, 523–551.

Clore, G. M., Martin, S. R., & Gronenborn, A. M. (1986b) *J. Mol. Biol. 191*, 553–561.

Clore, G. M., Nilges, M., Brunger, A., & Gronenborn, A. M. (1988) *Eur. J. Biochem. 171*, 479–484.

Davis, D. G., & Bax, A. (1985) *J. Am. Chem. Soc. 107*, 2820–2821.

DeGrado, W. F. (1983) in *Peptides: Structure and Function* (Hruby, V., & Rich, D. H., Eds.) pp 195–198, Pierce Chemical Co., Rockford, IL.

Di Stefano, D. L., & Wand, A. J. (1987) *Biochemistry 26*, 7272–7281.

Dykstra, R. (1987) *J. Magn. Reson. 72*, 162–167.

Dykstra, R., & Wand, A. J. (1987) *J. Magn. Reson. 75*, 158–161.

Edmunds, D. T. (1985) *Eur. Biophys. J. 13*, 31–35.

Fox, R. O., & Richards, F. M. (1982) *Nature (London) 300*, 325.

Fukushima, D., Kupferberg, J. P., Yokoyama, S., Kroon, D. J., Kaiser, E. T., & Kezdy, F. J. (1979) *J. Am. Chem. Soc. 101*, 3703–3704.

Gronenborn, A. M., Bovermann, G., & Clore, G. M. (1987) *FEBS Lett. 215*, 88–94.

Halstead, B. W. (1970) in *Poisonous and Venomous Marine Animals of The World*, Vol. 3, U.S. Government Printing Office, Washington, D.C.

Holak, T. A., Engstrom, A., Kraulis, P. J., Lindeberg, G., Bennick, H., Jones, T. A., Gronenborn, A. M., & Clore, G. M. (1988) *Biochemistry 27*, 7620–7629.

Harvey, S. C. (1989) *Proteins 5*, 78–92.

Jeener, J., Meier, B. H., Bachmann, P., & Ernst, R. R. (1979) *J. Chem. Phys. 71*, 4546–4553.

Kaiser, E. T., & Kezdy, F. J. (1987) *Annu. Rev. Biophys. Chem. 16*, 561–581.

Knoppel, E., Eisenberg, D., & Wickner, W. (1979) *Biochemistry 18*, 4177.

Lazarovici, P., Primor, N., & Loew, L. M. (1986) *J. Biol. Chem. 261*, 16704–16713.

Lazarovici, P., Primor, N., Gennaro, J., Fox, J., Shai, Y., Lelkes, P. I., Caratsch, C. G., Raghunathan, G., Gruy, H. R., Shih, Y. L., & Edwards, L. (1989) *Marine Toxins: Origins Structure and Pharmacology* (Hall, S., Ed.) ACS Symposium Series, Washington, D.C.

Marion, D., Zasloff, M., & Bax, A. (1988) *FEBS Lett. 227*, 21–26.

Merrifield, R. B. (1963) *J. Am. Chem. Soc. 85*, 2149–2154.

Mitchell, A. R., Kent, S. B. H., Engelhard, M., & Merrifield, R. B. (1978) *J. Org. Chem. 43*, 2845–2853.

Morris, G. A. (1986) *Magn. Reson. Chem. 24*, 371–403.

Otting, G., Widmer, H., Wagner, G., & Wuthrich, K. (1986) *J. Magn. Reson. 66*, 187–193.

Pardi, A., Hare, D. R., Selsted, M. E., Morrison, R. D., Bassolino, D. A., & Bach, A. C. (1988) *J. Mol. Biol. 201*, 625–636.

Primor, N. (1983) *J. Exp. Biol. 105*, 83–94.

Primor, N., & Zlotkin, E. (1975) *Toxicon 13*, 227–231.

Renner, P., Caratsch, C. G., Waser, P. G., Lazarovici, P., & Primor, N. (1987) *Neuroscience 23*, 319–325.

Riddick, J. A., & Bunger, W. B. (1970) in *Organic Solvents: Techniques of Organic Chemistry*, Vol. II, Wiley-Interscience, New York.

Schulz, G. E., & Schirmer, R. H. (1979) in *Principles of Protein Structure* (Cantor, C. R., Ed.) pp 108–110, Springer-Verlag, New York.

Schulze, J. (1987) *Biochim. Biophys. Acta. 901*, 101–111.

States, D. J., Haberkorn, R. A., & Ruben, D. J. (1982) *J. Magn. Reson. 48*, 286–292.

Tachibana, K., Xu, W. H., Barrow, C. J., & Imoto, S. (1989) in *Peptide Chemistry* (Ueki, M., Ed.) pp 279–284, Protein Research Foundation, Osaka, Japan.

Tappin, M. J., Pastore, A., Norton, R. S., Freer, J. H., & Campbell, I. D. (1988) *Biochemistry 27*, 1643–1647.

Terwillinger, T. C., & Eisenberg, D. (1982) *J. Biol. Chem. 257*, 6010–6015.

Thompson, S. A., Tachibana, K., Nakanishi, K., & Kubota, I. (1986) *Science 233*, 341–343.

Thompson, S. A., Minakata, M., Xu, W. H., Tachibana, K., Nakanishi, K., & Kubota, I. (1987) in *Peptide Chemistry* (Miyazawa, T., Ed.) pp 181–186, Protein Research Foundation, Osaka, Japan.

Thompson, S. A., Tachibana, K., Kubota, I., & Zlotkin, E. (1988) in *Peptide Chemistry* (Sakakibara, S., Ed.) pp 127–132, Protein Research Foundation, Osaka, Japan.

Tosteson, M. T., & Tosteson, D. (1982) *Biophys. J. 36*, 109–116.

Wagner, G., Braun, W., Havel, T. F., Schaumann, T., Go, N., & Wuthrich, K. (1987) *Biochemistry 27*, 4004–4012.

Wuthrich, K. (1986) *NMR of Proteins and Nucleic Acids*, Wiley, New York.

Wuthrich, K., Wider, G., Wagner, G., & Braun, W. (1982) *J. Mol. Biol. 155*, 311–319.

Zahuranec, B. J. (1983) in *Shark Repellents From The Sea: New Perspectives*, American Association for the Advancement of Science, Washington, D.C.